

A DNN Biophysics Model with Topological and Electrostatic Features

Elyssa Sliheet^a, Md Abu Talha^a, Weihua Geng^{a,*}

^a*Department of Mathematics, Southern Methodist University, Dallas, TX 75275 USA*

Abstract

In this project, we provide a deep-learning neural network (DNN) based biophysics model to predict protein properties. The model uses multi-scale and uniform topological and electrostatic features generated using protein structural information and force field. The topological features are generated using the element specified persistent homology (ESPH) on a selection of heavy atoms or carbon atoms which contribute significantly in the protein biophysical properties. The electrostatic features are fast computed using a Cartesian treecode, modulated with treecode parameters for accuracy-cost tradeoff. These features are uniform in number for proteins with various sizes thus the broadly available protein structure database can be used to train the network. These features are also multi-scale thus the resolution and computational cost can be balanced by the users at the consideration of available computing powers. The machine learning simulations on two data sets with 4000+ and 17000+ protein structures showed the efficiency and fidelity of these features in representing the protein structure and force field for the predication of their biophysical properties such as electrostatic Coulombic energies and solvation energies. The feature generation algorithms have the potential as general tools in assisting machine learning based biophysical properties and function prediction for the broad biomolecules whose structures are obtained from both theoretical computing and experiments.

Keywords: Electrostatics; Poisson-Boltzmann; treecode; Deep Neural Network; Persistent Homology

1. Introduction

One of the overarching themes of biology is that structure determines function, which becomes more significant when we explore the biological world at the molecular level. With the advancement and availability of structure determination techniques such as X-ray crystallography [1, 2], NMR spectroscopy [3], cryo-electron microscopy [4], etc., there are rapidly growing 3D structures of protein, nucleic acids, and complex assemblies, etc. on publicly accessible repository such as Protein Data Bank (PDB) [5], GenBank [6], etc. These structure determination techniques have strengths and limitations that make them suitable for different types research studies. For examples, X-ray crystallography, due to the requirement of crystallization, is best for static high-resolution structures. NMR is valuable for studying dynamics in solution, particularly for the studies of smaller proteins and complexes. Cryo-electron microscopy which becomes more and more popular recently, excels in visualizing large, complex, and flexible biomolecular systems. The combination and integration of these methods due to their complementary natures help to reveal critical biomolecular

*Corresponding author

Email addresses: esliheet@smu.edu (Elyssa Sliheet), atalha@smu.edu (Md Abu Talha), wgeng@smu.edu (Weihua Geng)

functions embedded in the structures.

In addition to experiments, computing approaches are also available for the prediction of protein structures and properties. The main stream of Machine Learning based protein prediction focuses on using amino acid sequence to predict protein structure or structure-related properties, resulting in the trending protein language models (PLM) [7, 8], which is a transformer-based model inspired by Natural Language Processing (NLP) with wide range of applications such as protein pKa prediction [9], protein structure prediction [10], protein design [11], protein evolution [12], etc.

Recently, the appearance of AlphaFold developed by Google DeepMind revolutionarily reshaped the structures determination techniques. Based on known structures, AlphaFold learned to predict protein’s structures from sequence with very high accuracy as shown by their victory by a large margin in Critical Assessment of Techniques for Protein Structure Prediction (CASP 14-16), AlphaFold Protein Structures Database now has over 200 million protein structure predictions [13].

Both PLM and AlphaFold take protein sequences as inputs to predict structures or embeddings which keep important features, without touching the prediction of protein functions from protein structures. The machine learning methods potentially can revolutionize the traditional structure-based molecular modeling, which uses brownian dynamics, molecular dynamics, Monte Carlo simulations, etc. to predict protein properties and functions from protein structures. However, the development of ML methods in protein property predictions is hindered by the difficulty to represent protein structures and force fields using reliable features. To this end, the structure data, which is largely variant from protein to protein, needs to be converted to uniform size of features in representing structures to be loaded into the machine learning models such as regression models, random forest, deep neural network etc. Successful cases are the use of graph convolutional network (GCN) for predicting protein functions by features extracted from a protein language model and protein structure [14], protein-DNA binding specificity prediction using a wide range of features from geometry [15, 16], protein-ligand binding affinity prediction using topological features, [17, 18].

In this paper, we provide a novel way to generate electrostatic features. Combining electrostatic features with the topological features generated using a modification of the persistent homology approach used in [19], we represent the protein structures and associated force field in a uniform and multiscale fashion. With these features, we train a deep-learning neural network (DNN) to predict protein Coulombic energy and electrostatic solvation energy efficiently and accurately. Here the Solvation energies as labels are generated by solving the Poisson-Boltzmann (PB) model using a second-order Matched Interface and Boundary (MIB) method based PB solver [20]. There are recent research using Physics Informed Neural Network (PINN) to solve the Poisson-Boltzmann model [21, 22] while the present work is rather different as a Data-driven method with uniform and multi-scale features. In addition to these particular application in predicting Coulombic energy and electrostatic solvation energy, the feature generation algorithm we have developed potentially has wider application for other machine learning models as far as the protein structures and force field are required to be represented uniformly for proteins with various sizes.

This manuscript is constructed in the following way. After this section of introduction is the section of models and algorithms, followed by the section of results of simulation. The manuscript is ended with a conclusion section.

2. Models and Algorithms

We introduce the models and algorithms involved in this work. For protein’s structure-property relation we focus on the atomic description and the electrostatic interactions. The protein properties involved in this paper are Coulombic energy E_{coul} and electrostatic solvation energy E_{solv} . For a protein, the Coulombic energy E_{coul} is the energy it takes to displace atomic charges of the protein

from infinity to their present positions (i.e. atomic centers from the PDB file) while the electrostatic solvation energy E_{solv} is the energy it takes to solvate the protein into the solvent (e.g. water). Formal quantitative definition of these two protein properties will be given with mathematical models. For the protein-solvent interaction, we use the implicit solvent model in which water is represented as a continuum for the reduced computational cost. In a comparison perspective, we introduce the two most popular implicit solvation models, namely the Poisson-Boltzmann model and the Generalized Born’s model, which are used to generate the labels or features. Following that, we introduce the persistent homology and how we use it to produce the topological features. Finally we introduce how to use the Cartesian treecode, whose modification evolves into the algorithm to generate the electrostatic features.

2.1. The Poisson-Boltzmann model

Figure 1 depicts the popular implicit solvent models. In Fig. 1(a) a protein is represented by a collection of N_c spherical atoms with centered partial charges. The molecular surface Γ (also known as the solvent excluded surface) is defined by the trace of a water molecule represented by a red sphere rolling on contacting with the protein atoms. The Poisson-Boltzmann model is shown in Fig. 1(b), where the molecular surface Γ divides the entire computational domain Ω into the protein domain Ω_1 with dielectric constant ϵ_1 and atomic charges q_k located at $\mathbf{x}_k, k = 1:N_c$, and the solvent domain Ω_2 with dielectric constant ϵ_2 and dissolved salt ions [23, 24]. Assuming a Boltzmann distribution for the ion concentration, and considering the case of two ion species with equal and opposite charges (e.g. Na^+, Cl^-), in the limit of weak electrostatic potential one obtains the linearized Poisson-Boltzmann (PB) model [25],

$$\epsilon_1 \nabla^2 \phi_1(\mathbf{x}) = - \sum_{k=1}^{N_c} q_k \delta(\mathbf{x} - \mathbf{x}_k), \quad \mathbf{x} \in \Omega_1, \quad (1a)$$

$$\epsilon_2 \nabla^2 \phi_2(\mathbf{x}) = \kappa^2 \phi_2(\mathbf{x}), \quad \mathbf{x} \in \Omega_2, \quad (1b)$$

$$\phi_1(\mathbf{x}) = \phi_2(\mathbf{x}), \quad \epsilon_1 \frac{\partial \phi_1}{\partial n}(\mathbf{x}) = \epsilon_2 \frac{\partial \phi_2}{\partial n}(\mathbf{x}), \quad \mathbf{x} \in \Gamma, \quad (1c)$$

where κ is the inverse Debye length measuring the salt concentration, and the potential satisfies a zero far-field boundary condition $\lim_{|\mathbf{x}| \rightarrow \infty} \phi(\mathbf{x}) = 0$.

The PB model governs the electrostatic potential ϕ in the entire space. Theoretically after ϕ is obtained, its gradient will produce electrostatic field while its integral will generate potential energy. However, there are many challenging issues on properly obtaining the field and energy (e.g. definition of field on molecular surface Γ [26]). Our attention for this project is on the energy side as described below. The electrostatic free energy is given as

$$E_{\text{free}} = \frac{1}{2} \int_{\Omega} \rho(\mathbf{x}) \phi(\mathbf{x}) d\mathbf{x} = \frac{1}{2} \sum_{k=1}^{N_c} q_k \phi(\mathbf{x}_k) = \frac{1}{2} \sum_{k=1}^{N_c} q_k (\phi_{\text{reac}}(\mathbf{x}_k) + \phi_{\text{coul}}(\mathbf{x}_k)) = E_{\text{solv}} + E_{\text{coul}} \quad (2)$$

where $\rho(\mathbf{x}) = \sum_{k=1}^{N_c} q_k \delta(\mathbf{x} - \mathbf{x}_k)$ is the charge density as a sum of partial charges weighted delta function and the $E_{\text{solv}} = \frac{1}{2} \sum_{k=1}^{N_c} q_k \phi_{\text{reac}}(\mathbf{x}_k)$ term is the electrostatic solvation energy. The $\phi_{\text{reac}}(\mathbf{x}_k)$ is the reaction potential at \mathbf{x}_k as the remaining component when Coulomb potential $\phi_{\text{coul}}(\mathbf{x}_k) = \sum_{j=1, j \neq k}^{N_c} \frac{q_j}{\epsilon_1 |\mathbf{x}_k - \mathbf{x}_j|}$ is taken away from the total electrostatic potential $\phi(\mathbf{x}_k)$.

Solving the PB model numerically by grid-based methods is challenging because (1) the protein is represented by singular point charges, (2) the molecular surface is geometrically complex, (3) the

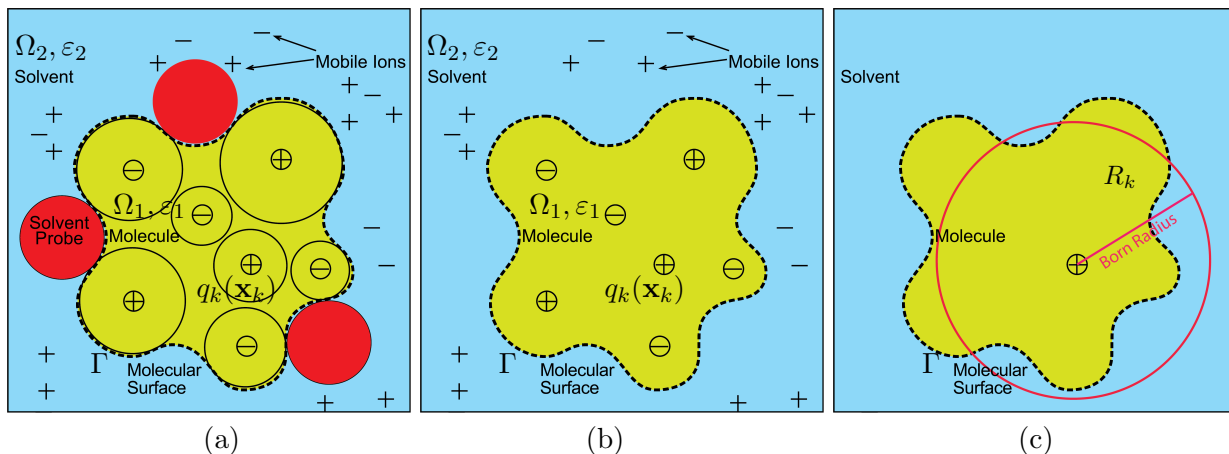


Figure 1: Implicit solvent models. (a) The Molecular Surface Γ : the trace of the solvent probe (shown in red) when it is rolled on contacting the spherical atoms of the protein (shown in green with a centered charge); (b) The Poisson–Boltzmann Model: two domains Ω_1 (dielectric constant ϵ_1 with partial charges as weighted summation of delta functions) and Ω_2 (dielectric constant ϵ_2 with mobile ions modeled by Boltzmann distribution) are separated by the molecular surface Γ ; (3) The Generalized Born Model: the protein is represented as a collection of N_c spherical atoms centered at \mathbf{x}_k with charge q_k and Born Radius R_k (only the k th atom is shown).

dielectric constant is discontinuous across the surface, (4) the domain is unbounded. To overcome these numerical difficulties, several finite difference interface methods have been developed. By assuming that the interface is aligned with a mesh line, a jump condition capture scheme has been developed in [27]. Based on a Cartesian grid, the immersed interface method (IIM) [28] has been applied to solve the PB equation [29, 30], in which the jump conditions can be rigorously enforced based on Taylor expansions. For the purpose of dealing with arbitrarily shaped dielectric interfaces based on a simple Cartesian grid, a matched interface and boundary (MIB) PB solver [20, 31–34] has been developed through rigorous treatments of geometrical and charge singularities. Alternatively, boundary element methods (BEM) for the PB model were developed later [35–42] with several inherent advantages, (1) only the molecular surface is discretized rather than the entire solute/solvent volume, (2) the atomic charges are treated analytically, (3) the interface conditions are accurately enforced, (4) the far-field boundary condition is imposed analytically, (5) the matrix-vector product in iterative methods can be accelerated by fast algorithms [43–46]. In this paper, we computed the solvation energies using the MIBPB solver [20] since accuracy is of critical importance for the generation of labels (E_{solV}) that will be used to train the neural network.

2.2. Generalized Born’s Model

If ion effects are not considered, the solvation energy and the reaction potential can also be efficiently computed by using the generalized Born’s (GB) model, an approximation to the Poisson’s model. The GB model has significantly reduced computational cost as opposed to the PB or Poisson models, whose solutions require solving a 3D partial differential equation. Although we did not use the GB model to produce any numerical results for this project, we describe the GB model for its relationship with the PB model and its potential usage in electrostatic interactions. In fact, the GB model can calculate the electrostatic solvation energy which can be used either as the label or as a feature [47, 48] in our machine learning framework. It can also produce the reaction potentials at the atomic center, which can be used to generate the second level of electrostatic features as shown in Fig. 3, which will be explained within that content.

To derive the GB model, we first adopt some classic results for electrostatics from Jackson’s textbook [49] (sec. 1.11). Using the analogue from discrete point charge distribution for continuous charge density distribution, the electrostatic free energy of a charged system with density distribution $\rho(\mathbf{r})$ takes the form

$$E_{\text{free}} = \frac{1}{2} \int \rho(\mathbf{r})\phi(\mathbf{r})d\mathbf{r} = \frac{1}{8\pi} \int \mathbf{E}(\mathbf{r}) \cdot \mathbf{D}(\mathbf{r})d\mathbf{r}$$

by using the Poisson equation $-\nabla^2\phi = \rho(\mathbf{r})/\epsilon$, the electric field $\mathbf{E} = -\nabla\phi$, and electric displacement $\mathbf{D} = \epsilon\mathbf{E}$.

Now consider assembling a charge q_i to the center of a sphere of radius a_i and the center is located at the origin. The sphere separates the domain with ϵ_1 for $r < a_i$ and ϵ_2 for $r > a_i$. The assembly takes the energy

$$E_{\text{free},i} = \frac{1}{8\pi} \int \frac{\mathbf{D} \cdot \mathbf{D}}{\epsilon} d\mathbf{r} \approx \frac{1}{8\pi} \int_{r < a_i} \frac{q_i^2}{r^4 \epsilon_1} d\mathbf{r} + \frac{1}{8\pi} \int_{r > a_i} \frac{q_i^2}{r^4 \epsilon_2} d\mathbf{r} \quad (3)$$

where the Coulomb field approximation $\mathbf{D} = \frac{q_i \mathbf{r}}{r^3}$ is used.

From a slightly different perspective as in Eq. (2), the electrostatic solvation energy is the energy difference when ϵ for $r > a_i$ changes from ϵ_1 (unsolvated) to ϵ_2 (solvated) given as

$$E_{\text{solv},i} = \frac{1}{8\pi} \left(\frac{1}{\epsilon_2} - \frac{1}{\epsilon_1} \right) \int_{r > a_i} \frac{q_i^2}{r^4} d\mathbf{r} = \left(\frac{1}{\epsilon_2} - \frac{1}{\epsilon_1} \right) \frac{q_i^2}{2a_i}. \quad (4)$$

This result is consistent with the Poisson-Boltzmann model of a solvated spherical cavity with centered charges as summarized in [50], which is a special case from Kirkwood’s derivation of a series of spherical harmonics for a spherical cavity containing arbitrary multiple charges [51]. If we treat the molecule as a collection of spherical atoms, using Eq. (4) the total electrostatic solvation energy is

$$E_{\text{solv}} = \frac{1}{2} \left(\frac{1}{\epsilon_2} - \frac{1}{\epsilon_1} \right) \left(\sum_{i=1}^N \frac{q_i^2}{a_i} + \sum_{j \neq i}^N \frac{q_i q_j}{r_{ij}} \right) \approx \frac{1}{2} \left(\frac{1}{\epsilon_2} - \frac{1}{\epsilon_1} \right) \sum_{i=1}^N \sum_{j=1}^N \frac{q_i q_j}{f_{ij}^{\text{GB}}} \quad (5)$$

where r_{ij} is the distance between the atomic centers of atoms i and j . Here the first equation of E_{solv} has two terms: a sum of individual Born’s terms and pairwise Coulombic terms. Note the *actual* molecule is better represented by a dielectric interface (e.g. solvent excluded surface (SES)) which separates inside domain Ω_1 and outside domain Ω_2 . The charge q_i is located at the center \mathbf{r}_i of a sphere with radius a_i . We assume Ω_1 contains all these spheres. The model using dielectric interface requires a step further as been approximated in the second equation in Eq. (5).

Here f_{ij}^{GB} is the effective Born radii ($i = j$) or effective interaction distance ($i \neq j$). Assuming the effective Born Radii R_i ’s are obtained, a popular estimation of f_{ij}^{GB} is:

$$f_{ij}^{\text{GB}}(r_{ij}) = (r_{ij}^2 + R_i R_j e^{\frac{-r_{ij}^2}{4R_i R_j}})^{\frac{1}{2}}$$

Note R_i depends not only on a_i , but also on radii and relative positions of all other atoms. The estimation of effective Born radii is an active research area [52]. From Poisson-Boltzmann theory, the *perfect* Born radii is given as

$$R_i = \frac{1}{2} \left(\frac{1}{\epsilon_2} - \frac{1}{\epsilon_1} \right) \frac{q_i}{E_{\text{solv},i}^{\text{PB}}}$$

with $E_{\text{solv},i}^{\text{PB}}$ as the electrostatic solvation energy from the PB model with all except i th charge muted. This PB-GB relationship can be seen in Fig. 1(c), in which the electrostatic solvation energy of the sphere equals that of the molecule, both with a charge at the atomic center. There are many approaches to approximate R_i and a typical one is the volume integration via quadrature as

$$R_i^{-1} = \frac{1}{4\pi} \int_{\Omega_2} \frac{q_i^2}{r^4} d\mathbf{r} = \frac{q_i^2}{a_i} - \frac{1}{4\pi} \int_{\Omega_1/B(\mathbf{r}_i, a_i)} \frac{q_i^2}{r^4} d\mathbf{r}.$$

2.3. Topological Features

This section involves many fundamental concepts in Algebraic Topology. We use *italic* fonts to emphasize important terms and use **bold** fonts to indicate their sequential definition if there are any. The fundamental task of topological data analysis is to extract *topological invariants* as the intrinsic features of the underlying space. For the prediction of protein properties, we expect the topological invariants such as independent components, rings, cavities, etc. carry useful information which cannot be discovered from geometric observation and measurement. This is realized by the aid of *homology*, a mathematical framework that assigns algebraic objects (groups) to a topological space to measure its shape, especially its holes in various dimensions. Below we briefly introduce the *simplicial homology* and the *persistent homology*, and their associated terms and definitions. Following that, we explain how these homologies and their computations with protein structures are used to generate topological features.

2.3.1. Simplicial Homology

Topological invariants in a discrete data set (e.g. the collection of atomic positions of a protein) can be studied using *simplicial homology* which uses a specific rule (e.g. the choice of proximity parameter ϵ and an associated procedure to determine the edges connecting the vertices) to identify *simplicial complexes* (will be defined later) from *simplexes*. Here the simplex represents the simplest possible polytope in any given dimension like point, line segment, triangle, tetrahedron, etc. Formally, A **k -simplex** is the convex hull of $k + 1$ affinely independent points v_0, v_1, \dots, v_k :

$$\sigma^k = \left\{ \sum_{i=0}^k \lambda_i v_i \mid \lambda_i \geq 0, \sum \lambda_i = 1 \right\}$$

Each subset of $m + 1$ of these vertices forms an **m -face** of the simplex, which is itself an m -simplex.

The **boundary** of a k -simplex $[v_0, \dots, v_k]$ is:

$$\partial_k[v_0, v_1, \dots, v_k] = \sum_{i=0}^k (-1)^i [v_0, \dots, \hat{v}_i, \dots, v_k]$$

where ∂_k is the boundary operator from k -chains to $(k-1)$ -chains and \hat{v}_i means vertex v_i is omitted. Here a **k -chain** is a *formal* linear combination of k -dimensional simplexes in a simplicial complex.

With the concepts of simplex, face, boundary, chain, etc., we can formally define that a **simplicial complex** K is a collection of simplices such that:

1. Every face of a simplex in K is also in K .
2. The intersection of any two simplices is either empty or a common face.

Thus, each simplicial complex corresponds to a topological space by “filling in” the simplexes and gluing them together along shared faces.

2.3.2. Persistent Homology

However, the simplicial homology of a complex associated to a point set at a particular proximity parameter ϵ is insufficient to characterize the signal or noise. This calls for the ideas of *filtration* and *persistent homology*, which can identify and connect complexes at different level of complexity and record the appearance and disappearance of the homology group. The importance of persistence is that given a parameterized family of spaces, topological features which persist over a significant parameter ranges are considered as *signal* while those with short-lived features are treated as *noise* [53]. To this end, we introduce the concept of **filtration**, which is a sequence of nested simplicial complexes:

$$\emptyset = K_0 \subseteq K_1 \subseteq \dots \subseteq K_n = K.$$

Each K_i is a simplicial complex, and the sequence grows over time or scale. Instead of computing just the k -**homology group** $H_k(K)$, which is an algebraic object capturing the k -dimensional holes in a topological space represented by a simplicial complex K , we compute $H_k(K_i)$ for each i and track features as the birth, death, and persistence of a homology class. Let $C_k(K)$ be the group of k -chains, and let

$$\dots \xrightarrow{\partial_{k+1}} C_k(K) \xrightarrow{\partial_k} C_{k-1}(K) \xrightarrow{\partial_{k-1}} \dots$$

be the sequence of boundary maps, the k -**homology group** of K is defined as:

$$H_k(K) = \frac{\ker(\partial_k)}{\text{im}(\partial_{k+1})}$$

where

- $\ker(\partial_k)$ is the group of k -cycles: $Z_k = \{c \in C_k \mid \partial_k(c) = 0\}$
- $\text{im}(\partial_{k+1})$ is the group of k -boundaries: $B_k = \{\partial_{k+1}(c) \mid c \in C_{k+1}\}$

Hence, the k -th homology group is the group of cycles modulo boundaries:

$$H_k = Z_k/B_k$$

Taking H_1 as an example, $Z_1 = \ker(\partial_1)$ collects 1-chains (formal sum of edges) without boundary points thus general loops, while $B_1 = \text{im}(\partial_2)$ collects boundaries of 2-chains (a collection of triangles) that bound a filled-in region thus trivial holes, $H_1 = Z_1/B_1$ is then the collection of actual holes in the space.

2.3.3. Feature Generation from Barcode

To make the topological features uniform and physically informed, we choose to use Element Specific Persistent Homology (ESPH) to extract topological features at different level of complexity. ESPH has been used for successfully predicting protein-ligand binding [19]. The main idea is to select atom elements, which form the cloud of points, using target problem related physical, chemical, and biological information. In this project, since solvation energy and Coulomb energy are highly related to the amino acid chains, we use two collections of cloud of points. One is the collection of all Carbon atoms, which form the backbone of amino acids. The other is the collection of all heavy atoms $\{C, N, O, S\}$, whose locations and interconnections are also critical in protein structures. Once the collections of cloud of points are determined and selected, the *barcode* [53] carrying persisting homology information of the cloud of points are produced. Here the **barcode** is a graphical representation of persistent homology as a collection of horizontal line segments in a plane whose horizontal axis corresponds to the proximity parameter and whose vertical axis

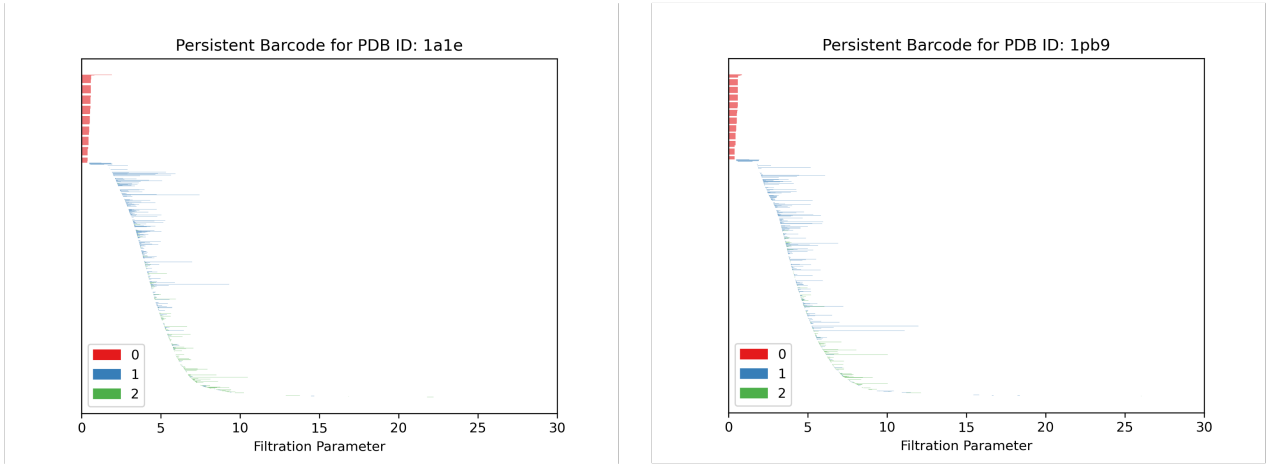


Figure 2: The barcode generated by the collection of cloud points using heavy atoms in proteins (a) 1a1e and (b) 1pb9.

represents an (arbitrary) ordering of homology generators such as H_0 , H_1 , H_2 , etc. We use the software GUDHI [54] to implement this task. The produced barcode is then used by the algorithm below to generate the vector of topological features.

Figure 2 gives the barcode for protein 1a1e, the C-SRC Tyrosine Kinase, and protein 1pb9, the N-methyl-D aspartate receptor, using heavy atoms. The persistent homology analysis conducted in this study characterizes key biophysical phenomena, including intermolecular interactions, solvation effects, and hydrophobicity. Topological features are extracted from Betti-1 and Betti-2 barcodes, where the birth, death, and persistence values are computed based on the spatial distribution of carbon atoms and all heavy atoms within the protein structure, resulting in a total of 12 feature channels. Features derived from all heavy atoms represent the geometric interactions between specific types of atoms in the protein, whereas those computed from carbon atoms primarily reflect hydrophobic interactions and indirectly capture solvation effects. The analysis is performed over a distance scale of 0 to 50Å, which is discretized into uniform bins of 0.50Å to ensure fine-grained resolution of topological patterns. The topological information included in the barcode can be converted to features with the following approach [19].

We define the collection of barcodes as $\mathbb{B}(\alpha, \mathcal{C}, \mathcal{D})$ with the following specifications.

α : atom labels (a specific way to obtain a collection of atoms i.e., all heavy atoms in protein, heavy atoms close to the ligand, atoms near the mutated residue, etc.)

\mathcal{C} : type of simplicial complex (i.e., Ribs or Cech)

\mathcal{D} : dimension (i.e., Betti-0, Betti-1, etc.)

Using the collection, the structured vectors \mathbf{V}^b , \mathbf{V}^d , and \mathbf{V}^p can be constructed to respectively describe the birth, death, and persistent patterns of the barcodes in various spatial dimensions. Practically, the filtration interval $[0, L]$ is divided into n equal length subintervals and the patterns are characterized on each subinterval. The description vectors using their i th component are defined as:

$$\begin{aligned}
 \mathbf{V}_i^b &= \|\{(b_j, d_j) \in \mathbb{B}(\alpha, \mathcal{C}, \mathcal{D}) \mid (i-1)L/n \leq b_j \leq iL/n\}\|, 1 \leq i < n, \\
 \mathbf{V}_i^d &= \|\{(b_j, d_j) \in \mathbb{B}(\alpha, \mathcal{C}, \mathcal{D}) \mid (i-1)L/n \leq d_j \leq iL/n\}\|, 1 \leq i < n, \\
 \mathbf{V}_i^p &= \|\{(b_j, d_j) \in \mathbb{B}(\alpha, \mathcal{C}, \mathcal{D}) \mid (i-1)L/n \geq b_j, iL/n \leq d_j\}\|, 1 \leq i < n,
 \end{aligned} \tag{6}$$

These vectors can be viewed as (1D) images whose pixel value is $\|\cdot\|$, the cardinality of the

set. Each pixel is specialized by i , α , \mathcal{C} , \mathcal{D} as indices of corresponding sets. In this project, $\alpha \in \{\text{all Carbon atoms in the protein, all heavy atoms in the protein}\}$, $\mathcal{C} = \text{Cech}$, $\mathcal{D} \in \{\text{Betti-1, Betti-2}\}$, resulting in 12 vectors with the choice of b, d, p . This barcode-based approach is comparable to the method of persistence imaging [55], which can be directly integrated into standard machine learning pipelines (e.g., SVMs, neural networks, etc.) but requires more preprocessing such as smoothing and discretization.

2.4. Electrostatic Features

2.4.1. Introduction

In most of the molecular simulations, including Monte Carlo simulation, Brownian Dynamics, Molecular Dynamics, etc., the electrostatic interactions are characterized by the partial charges assigned at the atomic centers. These partial charges are assigned according to the force fields, which are a set of mathematical equations and parameters used to calculate the potential energy of a molecule based on its atomic structure and interactions. The force fields are determined by experiment or quantum chemistry.

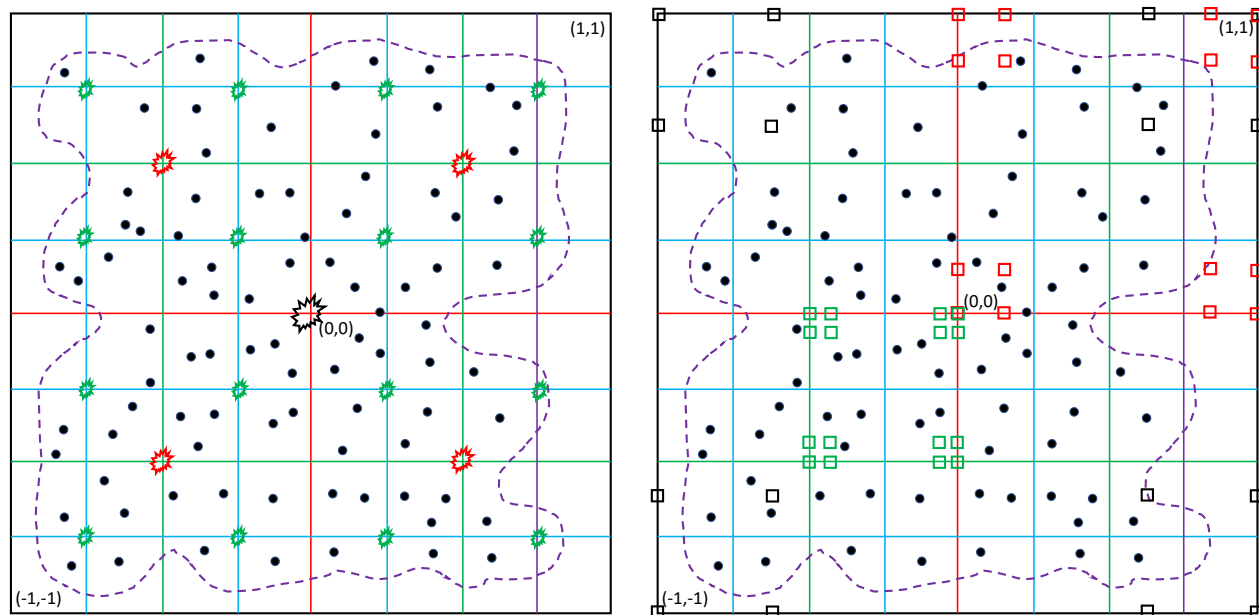


Figure 3: An 2-d illustration for 3-d uniform and multi-scale electrostatic features for a protein (purple dashed line) with charges (shown as black dots); left: charges q and reaction potential ϕ_{reac} are redistributed as point-multipoles (shown as explosion symbols) using Cartesian treecode [45] or FMM [46] at the centers of the cluster at different levels (level 0: black; level 1: red; level 2: green); right: charges q and reaction potential ϕ_{reac} are redistributed at Chebyshev nodes (shown as square: level 0: black; level 1: red; level 2: green; only one cluster is shown in each level) using Barycentric Lagrangian treecode [56].

The algorithm for obtaining the multi-scale, physics-informed, uniform electrostatic features can be explained using the left of Fig. 3. The electrostatic profile of the protein is determined by the partial charges $q_n(\mathbf{r}_n)$ or reaction potential $\phi_{\text{reac}}(\mathbf{r}_n)$ at the atomic centers \mathbf{r}_n 's as illustrated by the black dots for $n = 1, 2, \dots, N_c$ with N_c as the number of atoms of the protein. Partial charges are the source of electrostatic interactions while reaction potentials are the outcomes of electrostatic interactions for the solvated protein, which includes the important solute-solvent interactions. Consider the variation of N_c , the number of atoms, from protein to protein, it is difficult

to directly use $q_n(\mathbf{r}_n)$ and/or $\phi_{\text{reac}}(\mathbf{r}_n)$ as features for machine learning. Our strategy to alleviate this pain is to use point-multipoles as illustrated by the explosion symbols at the cluster centers to carry redistributed charges or reaction potentials in terms of moments of the multipole expansion. The number of cluster centers are uniform for proteins with various numbers of atoms. It is also multiscale as being determined by the combination of levels of the tree L and number of terms of the multipole expansion p . The users specify L and p as needed.

In the left of Fig. 3. the N_d point multipoles (explosion symbols) are organized in a hierarchical way such that different level of details are given by different number of symbols at different levels. For the m th multipole, $m = 1, \dots, N_d$, using a 3-d index $\mathbf{k} = (k_1, k_2, k_3)$, $|\mathbf{k}| = k_1 + k_2 + k_3$, in a cluster c with cluster center \mathbf{x}_c , the moments are defined as

$$\mathcal{M}_c^{\mathbf{k}} = \sum_{\mathbf{x}_j \in c} q_j(\mathbf{x}_j - \mathbf{x}_c)^{\mathbf{k}}. \quad (7)$$

Note when $|\mathbf{k}| = 0$, $\mathbf{k} = (0, 0, 0)$; when $|\mathbf{k}| = 1$, $\mathbf{k} \in \{(1, 0, 0), (0, 1, 0), (1, 0, 0)\}$; when $|\mathbf{k}| = 2$, $\mathbf{k} \in \{(1, 1, 0), (1, 0, 1), (0, 1, 1), (2, 0, 0), (0, 2, 0), (0, 0, 2)\}$, etc.

If the Cartesian treecode algorithm [45] is used, the computational cost is $O(N_c \log N_c)$ for obtaining all the moments as detailed in [45], where N_c is number of the particles/charges and $\log N_c$ is the level of trees. In fact, the computational cost can be as low as $O(N_c)$ using the strategies in [46] such that the moments at the finest cluster are computed first and a M2M (moments to moments) transformation can be used to efficiently compute moments at any desired level from the bottom to the top. Our simulations so far showed that the $O(N_c \log N_c)$ cost is sufficiently fast for moments computation since N_c is within the scale of tens of thousands even for large proteins. These moments are intrinsic properties of the cluster thus can serve as features for the protein, which carries simplified but important structural and charge information.

The number of features up to level L cluster (the largest box containing all particles is named as the level 0 cluster and each subdivision increases the level by 1) is

$$N_f(p, L) = N_p(1 + 8 + 8^2 + \dots + 8^L) = N_p \frac{8^{L+1} - 1}{7}$$

where N_p is the number of terms in multipole expansion with $N_p = 1, 4, 10, 20, 35, 56 \dots$ as the sequence of tetrahedral numbers when p th order multipole is used.

Alternatively, the Barycentric treecode approach as shown in the right picture of Fig. 3 can be used to generate the electrostatic features located the Chebyshev points (the squares) with *modified weights* as feature values. The details can be found in [56]. For this approach, the computational cost is $O(N_c \log N_c)$, and the number of terms in the similar sense of N_p is $O(c_p^3)$ where c_p is the number of Chebyshev nodes in one direction. In this project, we focus on the Cartesian treecode approach, while the Barycentric treecode approach will be investigated in the future.

2.4.2. Implementation details

We provide the step-by-step procedure by which the electrostatic features are generated.

Step 1. The protein structure (e.g. the PDB file) is obtained from publicly available repo e.g. the protein data bank [5]. The protein is represented by its atomic locations and partial charges: $q_i(\mathbf{r}_i)$ for $i = 1, \dots, N_c$, e.g. the PQR file using the PDB2PQR software [57].

Step 2. Two parameters p and L are given, where p is the order in the Cartesian Taylor expansion and L is the number of levels. With given p , we have the number of terms given as $N_p = (p+1)(p+2)(p+3)/6$. The number of features up to level L cluster is

$$N_f(p, L) = \frac{p(p+1)(p+2)(8^{L+1} - 1)}{42}.$$

These N_f numbers are ordered by level from 0 to L and the coordinates of cluster centers in each level. This determines the dimension of our final feature vector $F \in \mathbb{R}^{N_f}$.

The following table gives how N_f varies with the change of p and L :

$p \setminus L$	0	1	2	3	4
0	1	9	73	585	4681
1	4	36	292	2340	18724
2	10	90	730	5850	46810
3	20	180	1460	11700	93620
4	35	315	2555	20475	163835

Step 3. The Cartesian treecode [45] will be called and the moments for the multipoles will be output as the electrostatic features. These features can be used as part of the inputs for machine learning algorithms, which will be shown the next.

2.5. A DNN based machine learning model with topological and electrostatic features

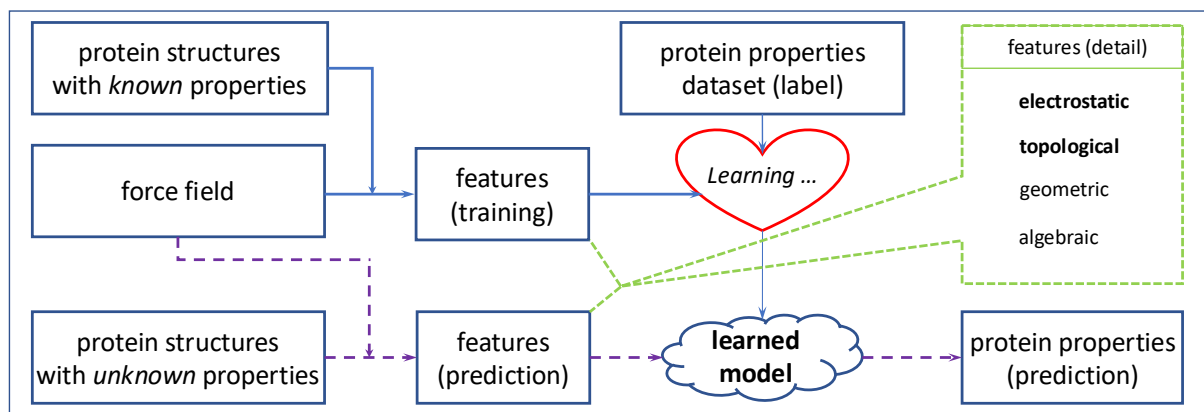


Figure 4: The DNN based Machine Learning model which uses protein structural data, force field, and known protein properties to mathematically generate electrostatic, topological, algebraic, geometric, and features to train a learned model and then use the learned model to predict unknown properties for protein with available structures.

The main goal of this project is to discover the hidden and useful information embedded in the protein structural data from the protein data bank in a simple and abstract way. The protein structure data and force field include bonded and non-bonded interactions with which the molecular simulation can be performed. We categorize these information into *electrostatic*, *topological*, *algebraic*, and *geometric* features. These four aspects are all important to the machine learning model. In this project, we put our focus on the electrostatic and topological features. The DNN based Machine Learning model is shown in Fig. 4, which uses the available protein structural data [58], force field such as AMBER [59], CHARMM[60], AMOEBA [61], etc. and known protein properties repositories such as PDBbind Database [62], Protein pKa Database [63], etc to mathematically generate features to train a learned model and then use the learned model to predict unknown properties for protein with available structures. In this project, we focus on the effectiveness of topological and electrostatic features using computed Coulombic energies and solvation free energies as labels.

3. Results

3.1. Specification of the machine learning model

We provide more details of the machine learning model with focus on the neural network and its related specification. The predictive model developed in this study is designed to predict solvation and Coulomb energies based on a combination of topological and electrostatic features. Prior to model training, outliers are identified and removed using the interquartile range (IQR) method. All input features and target labels are standardized to have zero mean and unit variance using the *StandardScaler()* utility from *sklearn.preprocessing*. The inverse transformations are applied to the output, returning values with physical meanings e.g. energies in kcal/mol during post-processing for evaluation purposes. The network architecture of the model as shown in Fig. 5 is implemented using the Keras Sequential API with two distinct branches. The first branch as color-coded in blue is a one-dimensional convolutional neural network (CNN) processing the topological features. The CNN branch has three convolution-pooling layers with (128, 64, 64) filters and (tanh, relu, tanh) activation function respectively. The 3 by 3 kernels are used. This CNN branch is responsible for capturing hierarchical and spatially correlated patterns in the topological data. The output of the CNN is flattened and passed through a subsequent Dense layer of 64 units. The other branch is the electrostatic features into two fully connected hidden dense layers with (128, 64) units respectively as shown in orange. After independent processing, the outputs from both branches are concatenated and passed through additional three hidden dense layers with (32, 16, 8) units as shown in purple to produce the final regression output of energy as shown in red.

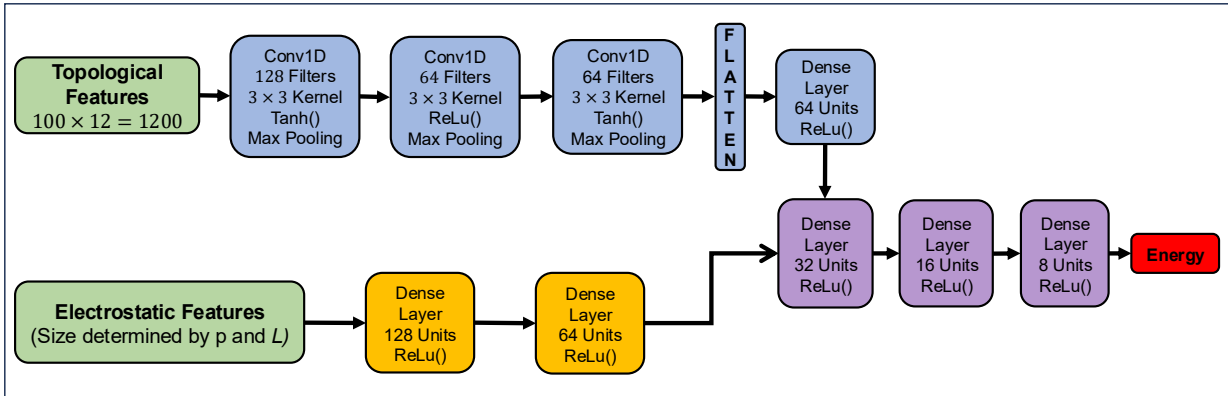


Figure 5: The architecture of the deep neural network with two branches taking in topological features and electrostatic features. The outputs of the two branches are concatenated into one deep neural network.

To enhance generalization and mitigate overfitting, batch normalization is applied after intermediate layers, and dropout is employed to randomly deactivate neurons during training. The model is trained for 500 epochs using the Adam optimizer with a learning rate of 0.0001 and a batch size of 32. The mean squared error (MSE) is used as a loss function. Model architecture and hyperparameters are selected through empirical tuning and informed by previous studies employing Hyperopt [19, 64]. The dataset as described below was split randomly into 80% for training and 20% for testing, and the model was trained with 5-fold cross-validation as well.

3.2. Data

The datasets are sourced from the PDBbind database [65]. In particular, we categorize used data into two datasets as described below. The Amber ff14SB general force field is applied for the

atomic van der Waals radii and partial charges when the PDB2PQR [57] software is used.

Dataset 1: These data are from the refined set of the v2018 release [65]. An interquartile range method is used to remove outliers based on E_{coul} , resulting in 4,658 complexes used in our simulation. We also we computed the electrostatic solvation free energies E_{solv} of the proteins, as part of the 4,658 protein-ligand complexes. All the E_{solv} values are computed using the 2nd order accurate Matched Interface and Boundary Poisson-Boltzmann (MIBPB) solver [20] at mesh size $h = 0.2\text{\AA}$.

Dataset 2: These data are from the the v2020 release, which has a general set with 14,127 complexes and refined set with 5,316 complexes. We computed the Coulomb energies E_{coul} of the all proteins using the Treecode [45]. An interquartile range method is used to remove outliers based on E_{coul} , resulting in 17,007 complexes used in our simulation.

3.3. Research Purposes and Metrics

We here provide some simulation results to demonstrate the performance of our model. These results serve three research purposes.

Purpose 1: Training on larger data set receives better performance.

Purpose 2: When electrostatic features are considered, performance of model improves when when treecode level L , Taylor expansion order p , and their associated number of features N_f increases.

Purpose 3: Using both electrostatic features and topological features outperforms using only one kind of these features.

Metrics: We use three common metrics to measure the performance of the model as defined below. In all these metrics, we use y_i to denote actual value, \hat{y}_i for predicted value, \bar{y} for mean of actual values, $\bar{\hat{y}}$ for mean of predicted values.

MAPE: The mean average percentage errors, which measures prediction accuracy as a percentage. Not suitable if the actual values contain zero or values close to zero.

$$\text{MAPE} = \frac{1}{n} \sum_{i=1}^n \left| \frac{y_i - \hat{y}_i}{y_i} \right| \times 100\%$$

MSE: The mean-squared error, which measures the average absolute difference between predicted and actual values.

$$\text{MSE} = \frac{1}{n} \sum_{i=1}^n (y_i - \hat{y}_i)^2$$

R^2 , which indicates the proportion of variance in the dependent variable that is predictable from the independent variables.

$$R^2 = 1 - \frac{\text{SS}_{\text{res}}}{\text{SS}_{\text{tot}}}$$

where $\text{SS}_{\text{tot}} = \sum_{i=1}^n (y_i - \bar{y})^2$ measures the total variance in the observed data and $\text{SS}_{\text{res}} = \sum_{i=1}^n (y_i - \hat{y}_i)^2$ measures the variance not explained by the model.

3.4. Performance

We next provide simulation results using different dataset and models. On reporting and explaining the performance of each combination of model and dataset, we focus on the achievement of the three aforementioned purposes.

E_{coul} computed using electrostatic features only on Dataset 1 and Dataset 2

We first investigate the effectiveness of electrostatic features in the prediction of the Coulombic energy E_{coul} . Note E_{coul} is determined by the location and charges of the particles, which also determines the moments of the multipoles as the electrostatic features.

Table 1: E_{coul} predicted using Electrostatic Features only on Dataset 1 and Dataset 2; D2-D1 indicates the difference of corresponding values of MSE and R^2 from Dataset 1 and Dataset 2.

p	L	$N_f(p, L)$	Dataset 1			Dataset 2			D2-D1		
			MSE	MAPE	R^2	MSE	MAPE	R^2	MSE	MAPE	R^2
1	0	4	0.641	0.328	0.351	0.682	0.532	0.331	0.041	0.204	-0.020
2	0	10	0.426	0.253	0.569	0.351	0.352	0.655	-0.074	0.100	0.086
3	0	20	0.352	0.206	0.643	0.252	0.318	0.753	-0.100	0.111	0.110
4	0	35	0.279	0.190	0.717	0.270	0.361	0.735	-0.009	0.172	0.018
0	1	9	0.699	0.354	0.292	0.663	0.548	0.349	-0.036	0.194	0.057
1	1	36	0.295	0.206	0.701	0.235	0.277	0.769	-0.060	0.070	0.068
2	1	90	0.284	0.175	0.712	0.154	0.224	0.848	-0.129	0.049	0.136
3	1	180	0.207	0.178	0.791	0.197	0.260	0.806	-0.009	0.082	0.016
4	1	315	0.203	0.157	0.794	0.224	0.320	0.780	0.021	0.163	-0.014
0	2	73	0.469	0.261	0.525	0.337	0.332	0.669	-0.131	0.071	0.144
1	2	292	0.249	0.182	0.748	0.144	0.201	0.859	-0.105	0.019	0.111
2	2	730	0.227	0.177	0.770	0.170	0.217	0.833	-0.057	0.040	0.063
3	2	1460	0.211	0.166	0.786	0.162	0.220	0.841	-0.049	0.054	0.055
4	2	2555	0.219	0.183	0.778	0.180	0.297	0.823	-0.039	0.114	0.045
0	3	585	0.465	0.265	0.529	0.287	0.283	0.719	-0.179	0.018	0.190
1	3	2340	0.513	0.220	0.480	0.255	0.259	0.750	-0.259	0.039	0.270
2	3	5850	0.469	0.230	0.525	0.215	0.240	0.789	-0.254	0.010	0.264
3	3	11700	0.450	0.220	0.544	0.269	0.248	0.736	-0.181	0.028	0.192
4	3	20475	0.451	0.221	0.543	0.241	0.323	0.764	-0.210	0.102	0.221

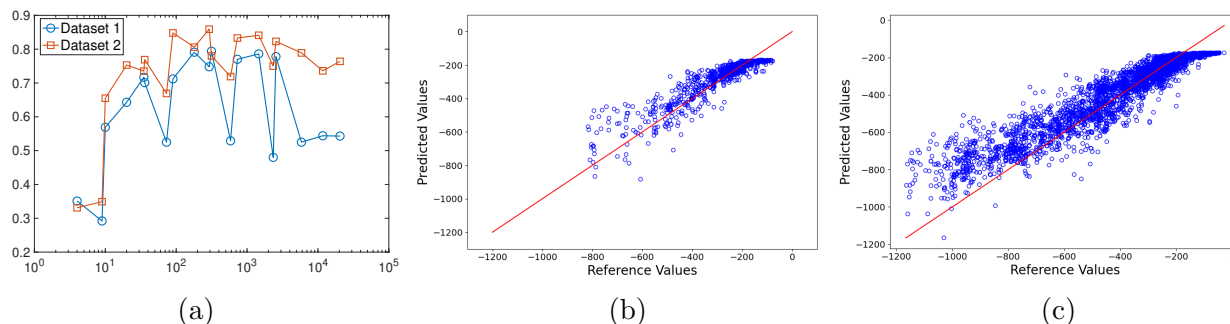


Figure 6: (a) R^2 of model performance against number of features; (b) scatter plot for Dataset 1 ($p = 4, L = 1$ with total 315 features); (c) scatter plot for Dataset 2 ($p = 1, L = 2$ with total 292 features)

Table 1 reports the E_{coul} prediction using electrostatic only on Dataset 1 and Dataset 2. The first important pattern we can observe from the table is that the MSE and R^2 obtained from Dataset 2 are essentially better than those obtained from Dataset 1 as the differences of MSE (D2-D1) are

almost all negative and the difference of R^2 (D2-D1) is almost all positive. This pattern validates **Purpose 2** indicating advantage of using larger dataset, particularly at capturing more overall variance in the target. We also noticed the difference of MAPE(D2-D1) is almost all positive, which apparently contradicts the results from MSE and R^2 . In fact, this gives more information about the data distribution, i.e. the data in Dataset 2 but not in Dataset 1 might contain more smaller target values, yielding large percentage errors.

Also from Table 1, we can see on Dataset 1, MSE decreases and R^2 increase with the increment of p and L , reaching optimized value at $p = 4$ and $L = 1$ with 315 features. Similarly on Dataset 2, MSE decreases and R^2 increases with the increment of p and L too, reaching optimized value at $p = 1$ and $L = 2$ with 292 features. This pattern validates the **Purpose 1** showing the advantage of using more features. However, we should aware that optimized p and L are affected by the size of the training dataset. When the number of features are larger than number of samples, increasing number of features might bring negative impact such as overfitting.

We plot R^2 in Fig. 6(a) with horizontal axis as number of features N_f from the third column of Table 1. The validation of **Purpose 1** is shown since blue squares are lower than the red ones. The validation of **Purpose 2** is also shown since markers of the same color contain an increasing pattern as number of features increase until there are too many features. We also plot the best cases on using both Datasets in Fig. 6(b,c) and we can see the distribution of the data points are essentially around the $\hat{y} = y$ line.

E_{coul} computed using e-features and both features on Dataset 2

Table 2: E_{coul} computed using e-features and both features on Dataset 2; the MSE and R^2 for using Topological Features only is 0.039 and 0.962 respectively.

p	L	$N(p, L)$	e-features		both features		difference	
			MSE	R^2	MSE	R^2	MSE	R^2
1	0	4	0.682	0.331	0.039	0.961	-0.643	0.631
2	0	10	0.351	0.655	0.033	0.967	-0.318	0.312
3	0	20	0.252	0.753	0.044	0.956	-0.208	0.203
4	0	35	0.270	0.735	0.030	0.970	-0.240	0.235
0	1	9	0.663	0.349	0.030	0.970	-0.634	0.621
1	1	36	0.235	0.769	0.040	0.960	-0.195	0.191
2	1	90	0.154	0.848	0.044	0.956	-0.110	0.108
3	1	180	0.197	0.806	0.037	0.963	-0.160	0.156
4	1	315	0.224	0.780	0.045	0.955	-0.179	0.175
0	2	73	0.337	0.669	0.048	0.952	-0.289	0.283
1	2	292	0.144	0.859	0.062	0.939	-0.082	0.080
2	2	730	0.170	0.833	0.051	0.949	-0.119	0.116
3	2	1460	0.162	0.841	0.032	0.969	-0.131	0.128
4	2	2555	0.180	0.823	0.039	0.961	-0.141	0.138
0	3	585	0.287	0.719	0.047	0.953	-0.240	0.235
1	3	2340	0.255	0.750	0.050	0.951	-0.205	0.201
2	3	5850	0.215	0.789	0.042	0.958	-0.172	0.169
3	3	11700	0.269	0.736	0.032	0.968	-0.236	0.232
4	3	20475	0.241	0.764	0.037	0.964	-0.204	0.200

We next investigate the effectiveness of combined features. This investigation has two parts. The first part is using E_{coul} as labels with Dataset 2 and the second part is using E_{solv} as labels with Dataset 1 considering the availability of labels and the size of the datasets. The MSE and R^2 for different models are shown in Table 2. Note the MSE and R^2 for using topological features only is 0.039 and 0.962 respectively, which is already very effective. If we see the difference column, we can see that adding topological features fundamentally improves the model using electrostatic features only by decreasing MSE and increase R^2 . This partially validates **purpose 2**. Note we did not report MAPE result here as it shows similar pattern as MSE does. If we consider topological features first, adding electrostatic features seems only occasionally improve the results. This is because the results from using topological features are too good for the effectiveness of electrostatic features to be kicked in. Our next test case shows when the topological features are relatively less effective, adding the electrostatic features can significantly improve the performance. Before we move to that case, let’s linger on Fig. 7, which is the scatter plot of predicted values vs true values for using topological features, electrostatic feature and combined feature, for the observation that the improvement from (b) to (c) are very obvious while the improvement from (a) to (c), although not that significant, is still discernible.

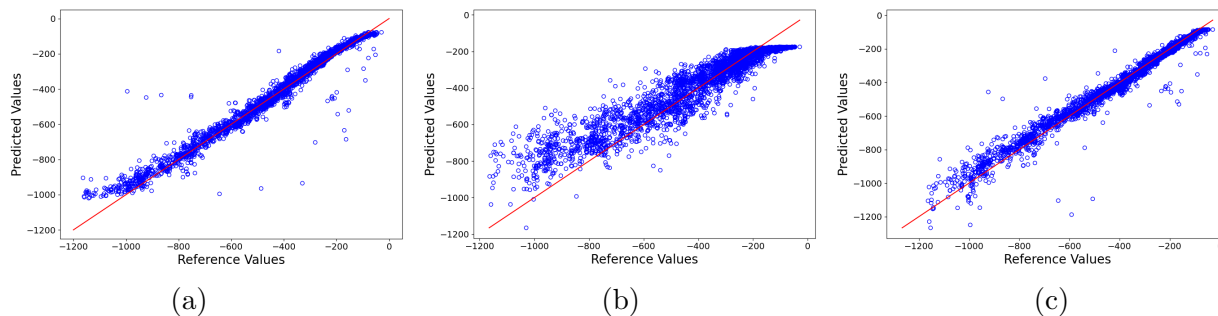


Figure 7: scatter plots: (a) topological features only, (b) e-features only ($p = 1, L = 2$ with total 292 features), (c) both features ($p = 4, L = 0$ with total 35 features).

E_{solv} computed using e-feature and both features on Dataset 1

As mentioned earlier, computing electrostatic solvation energies accurately is time consuming. Here we computed the solvation energies for the proteins from Dataset 1 using the MIBPB [20] solver. These solvation energies are used as labels for the neural network training and testing. A similar simulation using Dataset 1 are conducted and the results are reported in Table 3. From the table, we can see that the improvement on using both features from using topological features only or from using electrostatic features are significant. If we focus on the difference column (both features - e-features only), we can see adding topological features completely improve the model using electrostatic features only by decreasing MSE and increase R^2 . Meanwhile, the MSE and R^2 in the columns of using both features are obviously better than using topological feature only, which has $\text{MSE} = 0.150$ and $R^2 = 0.826$. These results validate **purpose 3**, showing the advantage of using topological and electrostatic features combined. Again, we did not report MAPE result here as it shows similar pattern as MSE does.

The optimized case for using e-feature only happens at $p = 1$ and $L = 1$ with 90 features. Adding topological features improve the performance. We provide the scatter plot between reference values and predicted values for using topological features only, electrostatic features only, and both features in Fig. 8. The improvements of using two kind of features as shown in (c) can be seen as compared with topological features only in (a) and electrostatic features only in (b).

Table 3: E_{solv} computed using e-features and both features on Dataset 1; the MSE and R^2 for using Topological Features only is 0.150 and 0.826 respectively.

p	L	$N(p, L)$	e-features		both features		difference	
			MSE	R^2	MSE	R^2	MSE	R^2
1	0	4	0.345	0.604	0.063	0.926	-0.282	0.323
2	0	10	0.271	0.690	0.090	0.895	-0.180	0.206
3	0	20	0.135	0.845	0.064	0.926	-0.071	0.081
4	0	35	0.121	0.861	0.065	0.925	-0.056	0.064
0	1	9	0.447	0.487	0.114	0.867	-0.333	0.380
1	1	36	0.148	0.830	0.077	0.911	-0.072	0.081
2	1	90	0.095	0.891	0.084	0.903	-0.012	0.012
3	1	180	0.111	0.873	0.105	0.878	-0.006	0.005
4	1	315	0.128	0.853	0.097	0.887	-0.031	0.034
0	2	73	0.214	0.754	0.092	0.892	-0.122	0.138
1	2	292	0.169	0.806	0.127	0.852	-0.041	0.045
2	2	730	0.164	0.812	0.128	0.851	-0.036	0.039
3	2	1460	0.212	0.757	0.138	0.839	-0.074	0.082
4	2	2555	0.218	0.750	0.165	0.808	-0.053	0.058
0	3	585	0.336	0.615	0.148	0.827	-0.188	0.213
1	3	2340	0.399	0.542	0.218	0.747	-0.181	0.205
2	3	5850	0.390	0.553	0.171	0.801	-0.219	0.249
3	3	11700	0.469	0.461	0.195	0.773	-0.275	0.312
4	3	20475	0.365	0.581	0.242	0.718	-0.123	0.137

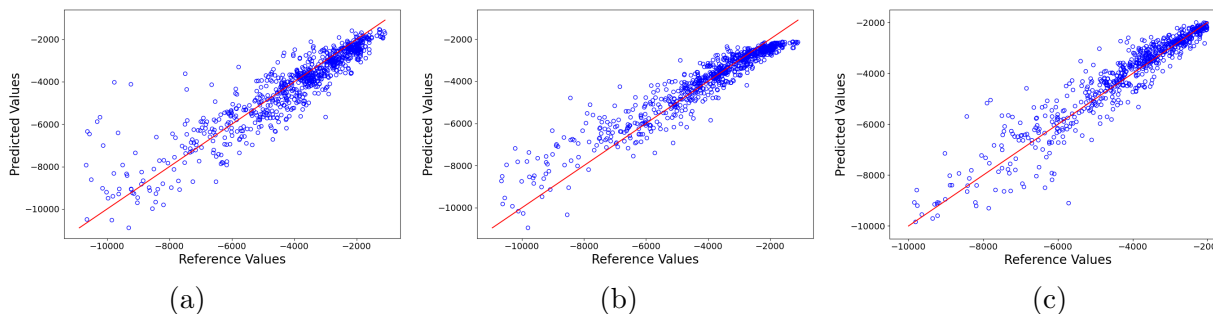


Figure 8: scatter plots: (a) topological features only, (b) e-features only ($p = 2, L = 1$ with total 90 features), (c) both features.

4. Software Dissemination

The code associated with this project is free and publically available on the GitHub deposit: https://github.com/atalha-cmd/Biophysics_ML.git maintained by SMU graduate student Md Abu Talha. It contains the Fortran code for generating the electrostatic features using Cartesian treecode, the Python code to generate topological features (a modified version as used in [19]), and the Python code for the neural network, which is originated from Elyssa Sliheet’s thesis work [66].

5. Conclusion

The project provides a novel approach to generate topological and electrostatic features combined to represent protein structures and charge distributions in a physical-informed multiscale and uniform way. Using these features, we can predict important protein properties such as the solvation energy and Coulombic energies. The numerical simulation validates our three purposes such that larger dataset, more electrostatic features, and combined features can improve the performance of the machine learning model. Other than predicting solvation energies and Coulomb energy, the resulting electrostatic and topological features potentially have broad usage as far as the proteins are needed to be represented in the forms of uniform and multiscale features for machine learning models. In the future, we will further investigate the role of reaction potential, which will be calculated using the much faster GB model as explained in the manuscript. We will also investigate Barycentric Lagrange treecode to generate electrostatic features as compared with the Cartesian treecode.

References

- [1] W. L. Bragg, "The specular reflection of x-rays," *Nature*, vol. 90, no. 2250, pp. 410–410, 1912.
- [2] D. Crowfoot, "X-ray single crystal photographs of insulin," *Nature*, vol. 135, no. 3415, pp. 591–592, 1935.
- [3] R. R. E. W. P. Aue, E. Bartholdi, "Two-dimensional spectroscopy. application to nuclear magnetic resonance.," *J. Chem. Phys.*, vol. 64, no. 5, p. 2229–2246, 1976.
- [4] Y. Cheng, N. Grigorieff, P. A. Penczek, and T. Walz, "A primer to single-particle cryo-electron microscopy," *Cell*, vol. 161, pp. 438–449, 2024/12/16 2015.
- [5] H. M. Berman, J. Westbrook, Z. Feng, G. Gilliland, T. N. Bhat, H. Weissig, I. N. Shindyalov, and P. E. Bourne, "The Protein Data Bank," *Nucleic Acids Research*, vol. 28, pp. 235–242, 01 2000.
- [6] D. A. Benson, M. Cavanaugh, K. Clark, I. Karsch-Mizrachi, D. J. Lipman, J. Ostell, and E. W. Sayers, "Genbank," *Nucleic Acids Research*, vol. 41, pp. D36–D42, 11 2012.
- [7] T. Bepler and B. Berger, "Learning the protein language: Evolution, structure, and function," *Cell Systems*, vol. 12, no. 6, pp. 654–669.e3, 2021.
- [8] K. Weissenow and B. Rost, "Are protein language models the new universal key?," *Current Opinion in Structural Biology*, vol. 91, p. 102997, 2025.
- [9] S. Xu and A. Onoda, "Accurate and rapid prediction of protein pka: Protein language models reveal the sequence-pka relationship," *Journal of Chemical Theory and Computation*, vol. 21, no. 7, pp. 3752–3764, 2025.
- [10] Z. Lin, H. Akin, R. Rao, *et al.*, "Evolutionary-scale prediction of atomic-level protein structure with a language model," *Science*, vol. 379, no. 6637, pp. 1123–1130, 2023.
- [11] A. Madani, B. Krause, E. R. Greene, *et al.*, "Large language models generate functional protein sequences across diverse families," *Nature Biotechnology*, vol. 41, no. 8, pp. 1099–1106, 2023.
- [12] Z. Zhang, H. K. Wayment-Steele, G. Brixi, H. Wang, D. Kern, and S. Ovchinnikov, "Protein language models learn evolutionary statistics of interacting sequence motifs," *Proceedings of the National Academy of Sciences U.S.A.*, vol. 121, no. 45, p. e2406285121, 2024.
- [13] J. Abramson, J. Adler, J. Dunger, R. Evans, T. Green, A. Pritzel, O. Ronneberger, L. Willmore, A. J. Ballard, J. Bambrick, S. W. Bodenstein, D. A. Evans, C.-C. Hung, M. O'Neill, D. Reiman, K. Tunyasuvunakool, Z. Wu, A. Žemgulytė, E. Arvaniti, C. Beattie, O. Bertolli, A. Bridgland, A. Cherepanov, M. Congreve, A. I. Cowen-Rivers, A. Cowie, M. Figurnov, F. B. Fuchs, H. Gladman, R. Jain, Y. A. Khan, C. M. R. Low, K. Perlin, A. Potapenko, P. Savy, S. Singh, A. Stecula, A. Thillaisundaram, C. Tong, S. Yakneen, E. D. Zhong, M. Zielinski, A. Židek, V. Bapst, P. Kohli, M. Jaderberg, D. Hassabis, and J. M. Jumper, "Accurate structure prediction of biomolecular interactions with alphafold 3," *Nature*, vol. 630, no. 8016, pp. 493–500, 2024.
- [14] V. Gligorijević, P. D. Renfrew, T. Kosciolk, J. K. Leman, D. Berenberg, T. Vatanen, C. Chandler, B. C. Taylor, I. M. Fisk, H. Vlamakis, R. J. Xavier, R. Knight, K. Cho, and R. Bonneau, "Structure-based protein function prediction using graph convolutional networks," *Nature Communications*, vol. 12, no. 1, p. 3168, 2021.

- [15] J. M. Sagendorf, R. Mitra, J. Huang, X. S. Chen, and R. Rohs, "Structure-based prediction of protein-nucleic acid binding using graph neural networks," *Biophysical Reviews*, vol. 16, no. 3, pp. 297–314, 2024.
- [16] R. Mitra, A. S. Cohen, W. Y. Tang, *et al.*, "Rnaprodb: A webserver and interactive database for analyzing protein-rna interactions," *Journal of Molecular Biology*, p. 169012, 2025.
- [17] B. Wang, Z. Zhao, D. Nguyen Duc, and G.-W. Wei, "Feature functional theory - binding predictor (fft-bp) for the blind prediction of binding free energies," *Theoretical Chemistry Accounts*, vol. 136, 04 2017.
- [18] J. Wee and K. Xia, "Persistent spectral based ensemble learning (perspect-el) for protein-protein binding affinity prediction," *Briefings in Bioinformatics*, vol. 23, no. 2, p. bbac024, 2022.
- [19] Z. Cang and G.-W. Wei, "Topologynet: Topology based deep convolutional and multi-task neural networks for biomolecular property predictions," *PLOS Computational Biology*, vol. 13, pp. 1–27, 07 2017.
- [20] D. Chen, Z. Chen, C. Chen, W. Geng, and G. W. Wei, "MIBPB: A software package for electrostatic analysis," *J. Comput. Chem.*, vol. 32, pp. 657–670, 2011.
- [21] M. A. Achondo, J. H. Chaudhry, and C. D. Cooper, "An investigation of physics informed neural networks to solve the poisson-boltzmann equation in molecular electrostatics," *Journal of Chemical Theory and Computation*, vol. 21, pp. 3726–3744, 04 2025.
- [22] D. Chen, C. He, X. Hu, L. Mu, and Z. Shen, "Deep Neural Network for Solving Poisson-Boltzmann Equations on Protein Surfaces," *Journal of Machine Learning for Modeling and Computing*, vol. 6, no. 1, pp. 41–63, 2025.
- [23] F. M. Richards, "Areas, volumes, packing, and protein structure," *Annu. Rev. Biophys. Bioeng.*, vol. 6, no. 1, pp. 151–176, 1977.
- [24] M. L. Connolly, "Depth buffer algorithms for molecular modeling," *J. Mol. Graphics*, vol. 3, pp. 19–24, 1985.
- [25] N. A. Baker, "Improving implicit solvent simulations: a Poisson-centric view," *Curr. Opin. Struct. Biol.*, vol. 15, no. 2, pp. 137–43, 2005.
- [26] W. Geng and G. W. Wei, "Multiscale molecular dynamics using the matched interface and boundary method," *J Comput. Phys.*, vol. 230, no. 2, pp. 435–457, 2011.
- [27] I. L. Chern, J.-G. Liu, and W.-C. Weng, "Accurate evaluation of electrostatics for macromolecules in solution," *Methods and Applications of Analysis*, vol. 10, no. 2, pp. 309–28, 2003.
- [28] R. LeVeque and Z. Li, "The immersed interface method for elliptic equations with discontinuous coefficients and singular sources," *SIAM J. Numer. Anal.*, vol. 31, no. 4, pp. 1019–1044, 1994.
- [29] Z. Qiao, Z. Li, and T. Tang, "Finite difference scheme for solving the nonlinear poisson-boltzmann equation modeling charged spheres," *Journal of Computational Mathematics*, vol. 24, 04 2006.

- [30] J. Wang, Q. Cai, Z.-L. Li, H.-K. Zhao, and R. Luo, “Achieving energy conservation in poisson-boltzmann molecular dynamics: Accuracy and precision with finite-difference algorithms,” *Chemical Physics Letters*, vol. 468, no. 4, pp. 112 – 118, 2009.
- [31] Y. C. Zhou, S. Zhao, M. Feig, and G. W. Wei, “High order matched interface and boundary method for elliptic equations with discontinuous coefficients and singular sources,” *J. Comput. Phys.*, vol. 213, no. 1, pp. 1–30, 2006.
- [32] S. Yu, W. Geng, and G. W. Wei, “Treatment of geometric singularities in implicit solvent models,” *J. Chem. Phys.*, vol. 126, p. 244108, 2007.
- [33] W. Geng, S. Yu, and G. W. Wei, “Treatment of charge singularities in implicit solvent models,” *J. Chem. Phys.*, vol. 127, p. 114106, 2007.
- [34] W. Geng and S. Zhao, “A two-component Matched Interface and Boundary (MIB) regularization for charge singularity in implicit solvation,” *J. Comput. Phys.*, vol. 351, pp. 25–39, 2017.
- [35] R. J. Zauhar and R. S. Morgan, “The rigorous computation of the molecular electric potential,” *J. Comput. Chem.*, vol. 9, no. 2, pp. 171–187, 1988.
- [36] A. Juffer, B. E., B. van Keulen, A. van der Ploeg, and H. Berendsen, “The electric potential of a macromolecule in a solvent: a fundamental approach,” *J. Comput. Phys.*, vol. 97, pp. 144–171, 1991.
- [37] J. Liang and S. Subramaniam, “Computation of molecular electrostatics with boundary element methods,” *Biophys. J.*, vol. 73, pp. 1830–1841, 1997.
- [38] A. H. Boschitsch, M. O. Fenley, and H.-X. Zhou, “Fast boundary element method for the linear Poisson-Boltzmann equation,” *J. Phys. Chem. B*, vol. 106, no. 10, pp. 2741–2754, 2002.
- [39] A. J. Bordner and G. A. Huber, “Boundary element solution of the linear Poisson-Boltzmann equation and a multipole method for the rapid calculation of forces on macromolecules in solution,” *J. Comput. Chem.*, vol. 24, no. 3, pp. 353–367, 2003.
- [40] B. Lu, X. Cheng, and J. A. McCammon, “A new-version-fast-multipole-method-accelerated electrostatic calculations in biomolecular systems,” *J. Comput. Phys.*, vol. 226, no. 2, pp. 1348 – 1366, 2007.
- [41] W. Geng and R. Krasny, “A treecode-accelerated boundary integral Poisson-Boltzmann solver for electrostatics of solvated biomolecules,” *J. Comput. Phys.*, vol. 247, pp. 62 – 78, 2013.
- [42] J. Chen, J. Tausch, and W. Geng, “A Cartesian FMM-accelerated Galerkin boundary integral Poisson-Boltzmann solver,” *Journal of Computational Physics*, vol. 478, p. 111981, 2023.
- [43] J. Barnes and P. Hut, “A hierarchical $O(N \log N)$ force-calculation algorithm,” *Nature*, vol. 324, pp. 446–449, 12 1986.
- [44] L. Greengard and V. Rokhlin, “A fast algorithm for particle simulations,” *J. Comput. Phys.*, vol. 73, no. 2, pp. 325 – 348, 1987.
- [45] P. Li, H. Johnston, and R. Krasny, “A Cartesian treecode for screened Coulomb interactions,” *J. Comput. Phys.*, vol. 228, pp. 3858–3868, 2009.

- [46] J. Tausch, “The fast multipole method for arbitrary Green’s functions,” *Contemporary Mathematics*, vol. 329, pp. 307–314, 2003.
- [47] J. Chen, W. Geng, and G.-W. Wei, “MLIMC: Machine learning-based implicit-solvent Monte Carlo,” *Chinese Journal of Chemical Physics*, vol. 34, no. 6, pp. 683–694, 2021.
- [48] J. Chen, Y. Xu, X. Yang, Z. Cang, W. Geng, and G.-W. Wei, “Poisson-Boltzmann-based machine learning model for electrostatic analysis,” *Biophysical Journal*, 2024/05/24 2024.
- [49] J. D. Jackson, *Classical Electrodynamics*. John Wiley & Sons, Inc., 1999.
- [50] W. Geng, “A boundary integral Poisson–Boltzmann solvers package for solvated bimolecular simulations,” *Computational and Mathematical Biophysics*, vol. 3, pp. 43–58, 2015.
- [51] J. G. Kirkwood, “Theory of solution of molecules containing widely separated charges with special application to zwitterions,” *J. Comput. Phys.*, vol. 7, pp. 351 – 361, 1934.
- [52] A. Onufriev, D. A. Case, and D. Bashford, “Effective born radii in the generalized born approximation: The importance of being perfect,” *Journal of Computational Chemistry*, vol. 23, no. 14, pp. 1297–1304, 2002.
- [53] R. Ghrist, “Barcodes: The persistent topology of data,” *Bulletin of the American Mathematical Society*, vol. 45, no. 1, pp. 61–75, 2007.
- [54] J.-D. Boissonnat and C. Maria, “The simplex tree: An efficient data structure for general simplicial complexes,” *Algorithmica*, vol. 70, no. 3, pp. 406–427, 2014.
- [55] H. Adams, T. Emerson, M. Kirby, R. Neville, C. Peterson, P. Shipman, S. Chepushtanova, E. Hanson, F. Motta, and L. Ziegelmeier, “Persistence images: A stable vector representation of persistent homology,” *Journal of Machine Learning Research*, vol. 18, no. 8, pp. 1–35, 2017.
- [56] L. Wang, R. Krasny, and S. Tlupova, “A kernel-independent treecode based on barycentric Lagrange interpolation,” *Commun. Comput. Phys.*, vol. 28, pp. 1415–1436, 2020.
- [57] T. J. Dolinsky, P. Czodrowski, H. Li, J. E. Nielsen, J. H. Jensen, G. Klebe, and N. A. Baker, “PDB2PQR: expanding and upgrading automated preparation of biomolecular structures for molecular simulations,” *Nucleic Acids Res.*, vol. 35, 2007.
- [58] <http://www.rcsb.org/pdb/home/home.do>.
- [59] D. A. Perlman, D. A. Case, J. W. Caldwell, W. S. Ross, T. E. Cheatham, S. Debolt, D. Ferguson, G. Seibel, and P. Kollman, “AMBER, a package of computer programs for applying molecular mechanics, normal mode analysis, molecular dynamics and free energy calculations to simulate the structural and energetic properties of molecules,” *Comp. Phys. Commun.*, vol. 91, pp. 1–41, 1995.
- [60] B. R. Brooks, R. E. Bruccoleri, B. D. Olafson, D. States, S. Swaminathan, and M. Karplus, “CHARMM: A program for macromolecular energy, minimization, and dynamics calculations,” *J. Comput. Chem.*, vol. 4, pp. 187–217, 1983.
- [61] C. Zhang, C. Lu, Z. Jing, C. Wu, J.-P. Piquemal, J. W. Ponder, and P. Ren, “Amoeba polarizable atomic multipole force field for nucleic acids,” *J. Chem. Theory Comput.*, vol. 14, pp. 2084–2108, 04 2018.

- [62] M. Su, Q. Yang, Y. Du, G. Feng, Z. Liu, Y. Li, and R. Wang, “Comparative assessment of scoring functions: The casf-2016 update,” *Journal of Chemical Information and Modeling*, vol. 59, pp. 895–913, 02 2019.
- [63] S. Pahari, L. Sun, and E. Alexov, “PKAD: a database of experimentally measured pKa values of ionizable groups in proteins,” *Database: Journal of Biological Databases and Curation*, vol. article ID baz024, pp. 1–7, Jan 2019.
- [64] J. Bergstra, B. Komer, C. Eliasmith, D. Yamins, and D. D. Cox, “Hyperopt: A python library for model selection and hyperparameter optimization,” *Computational Science & Discovery*, vol. 8, no. 1, p. 014008, 2015.
- [65] Z. Liu, Y. Li, L. Han, J. Li, J. Liu, Z. Zhao, W. Nie, Y. Liu, and R. Wang, “PDB-wide collection of binding data: current status of the PDBbind database,” *Bioinformatics*, vol. 31, pp. 405–412, 10 2014.
- [66] E. Sliheet, *Predicting Biomolecular Properties and Interactions Using Numerical, Statistical and Machine Learning Methods*. PhD thesis, Southern Methodist University, 2024.